

# Positron emission tomography detector performance with different crystal pitches

LinGe Tong<sup>1</sup> · YaMing Fan<sup>1</sup> · Ming Dong<sup>1</sup> · Liang Zhao<sup>1</sup> · ZhongXing Li<sup>1</sup> · YingGuo Li<sup>1</sup> · TianQuan Wang<sup>1</sup> · YongZhi Yin<sup>1</sup>  · XiMeng Chen<sup>1</sup>

Received: 19 August 2017 / Revised: 22 October 2017 / Accepted: 30 October 2017 / Published online: 14 November 2017

© Institute of High Energy Physics, Chinese Academy of Sciences; China Nuclear Electronics and Nuclear Detection Society and Springer Nature Singapore Pte Ltd. 2017

## Abstract

**Aims:** In this work, we evaluated the performance of three pitches positron emission tomography (PET) detectors for building a high-resolution small-animal PET imaging experimental platform.

**Methods:** The evaluation of PET detectors includes two-dimensional crystal identification, energy resolution, and crystal look-up table. The nuclear instrumentation module and PXI data acquisition (DAQ) system were both used to obtain flood images. The energy spectrum of the Na-22 source was measured. PET detectors of 2.0 and 1.6 mm pitches used in our present experiment were composed of lutetium yttrium oxyorthosilicate (LYSO) crystals directly coupled to position-sensitive photomultiplier tubes (PSPMTs). The 1.3-mm pitch detector comprises a LYSO crystal, a tapered light-guide, and a PSPMT. The crystal sizes of the detectors were a  $10 \times 10$  array of  $2.0 \times 2.0 \times 10 \text{ mm}^3$  crystals, a  $10 \times 10$  array of  $1.6 \times 1.6 \times 10 \text{ mm}^3$  crystals, and an  $18 \times 18$  array of  $1.3 \times 1.3 \times 10 \text{ mm}^3$  crystals, respectively. Due to the lower sampling frequency of the DAQ system, a spline interpolation algorithm was introduced in the signal waveform to reconstruct the peak values.

**Results:** The experimental results indicated that all three PET detector crystals could be clearly identified. A detailed analysis demonstrated that the key characteristic full width at half maximum (FWHM) values of the crystals profile could reach  $0.46 \pm 0.03$ ,  $0.32 \pm 0.03$ , and  $0.21 \pm 0.02$  mm, while the crystal average energy resolutions were  $16.8\% \pm 1.76\%$ ,  $20.1\% \pm 2.24\%$ , and  $31.5\% \pm 3.76\%$ , which correspond to

pitches of 2.0-, 1.6-, and 1.3-mm, respectively.

**Conclusions:** The PET detector modules of LYSO crystal arrays could be potentially used in the small-animal PET imaging applications and are promising to achieve sub-millimeter PET images.

**Keywords** PET detector · Flood image · Crystal look-up table

## Introduction

Since the onset of the twenty-first century, imaging techniques in nuclear medicine has been developed significantly and widely used in medical clinical diagnosis: single photon emission computed tomography (SPECT), positron emission tomography computed tomography (PET-CT), and PET-magnetic resonance imaging (PET-MRI) [1]. The principle of PET entails using a machine to detect pairs of gamma rays emitted indirectly by a positron-emitting radionuclide, which is introduced into a live subject on a biologically active molecule. The three-dimensional (3D) images are then reconstructed by certain algorithms. PET overcomes the shortcomings of planar imaging and is considered as a milestone in the history of nuclear medicine [2].

Most of the detector materials used in PET have been scintillators. The ideal scintillator should have the following advantages: high density, high effective atomic number, high light yield, short light decay time, and good energy resolution, etc. Many kinds of scintillation crystals have been used in PET detectors, including thallium doped with sodium iodide (NaI(Tl)), bismuth germanate (BGO), gadolinium oxyorthosilicate (GSO), lutetium oxyorthosilicate (LSO), lutetium–yttrium oxyorthosilicate (LYSO), and lanthanum

✉ YongZhi Yin  
yinyzh@lzu.edu.cn

<sup>1</sup> School of Nuclear Science and Technology, Lanzhou University, Lanzhou 730000, China

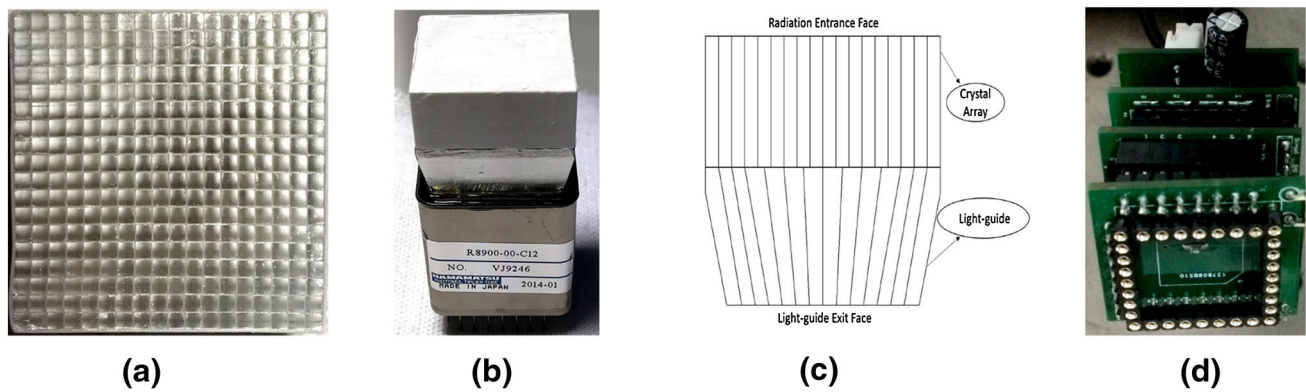


**Fig. 1** **a** 1.3-mm pitch LYSO crystal array, **b** an assembled 1.3-mm pitch PET detector, **c** cross-sectional view of the 1.3-mm pitch detector  $18 \times 18$  crystal array coupled to the  $14 \times 14$  element tapered light-guide, **d** readout circuits of R8900-C12 PSPMTs

bromide ( $\text{LaBr}_3$ ) [3–6]. Among these scintillators, LYSO has been the first choice in state-of-the-art PET detector design, especially in TOF-PET imaging applications.

In this paper, we characterized three LYSO detectors, which will be used to build a high-resolution small-animal PET. The detail evaluation of the performance of LYSO detectors includes 2D crystal identification, energy resolution, and crystal look-up table.

## Experimental setup

### Modular construction of the PET detector

Three kinds of LYSO crystals were used. The size of the crystal elements are  $2.0 \times 2.0 \times 10$ ,  $1.6 \times 1.6 \times 10$ , and  $1.3 \times 1.3 \times 10 \text{ mm}^3$ . The 2.0- and 1.6-mm pitch crystal arrays were  $10 \times 10$ , and the 1.3-mm pitch crystal arrays were  $18 \times 18$ . Each side of the LYSO crystals were polished, and the front and side surfaces were wrapped in white Teflon [7]. The PET detectors modular of 2.0- and 1.6-mm pitch were directly coupled to position-sensitive photomultiplier tubes (PSPMT, Hamamatsu R8900-C12). The 1.3-mm pitch detector  $18 \times 18$  crystal array was coupled to a  $14 \times 14$  element tapered light-guide, shown in Fig. 1.

The R8900-C12 PSPMT has a large detection area of  $23.5 \times 23.5 \text{ mm}^2$ . However, the PSPMT side is a concave arc, and the linear position response area for the incident photon is only  $21.5 \times 21.5 \text{ mm}^2$  [8]. This indicates that the photons generated in the edge crystals in the 1.3-mm-pitch detector could not be processed by the PSPMT dynodes.

A  $14 \times 14$  tapered light-guide was designed to deliver the photons from  $18 \times 18$  LYSO crystals into the PSPMT [9, 10]. The top entrance size of the light-guide remains the same with the scintillator array crystal area ( $23.5 \times 23.5 \text{ mm}^2$ ). The exit size of the light-guide was  $20.7 \times 20.7 \text{ mm}^2$ , the length was 10.5 mm and the reflectors was 0.1 mm  $\text{BaSO}_4$ . This design

enables all  $18 \times 18$  scintillator array crystal to be read out on effective detection area photocathode of the PSPMT.

The light-guide features  $9:4 (3 \times 3:2 \times 2)$  multiplexed coupling of the center 144 ( $12 \times 12$ ) scintillator array elements to corresponding light-guide elements, and features  $1:1 (1 \times 1:1 \times 1)$  multiplexed coupling of the three lines edge 180 scintillator array elements to corresponding light-guide elements. The pitch of light-guide center element size exit ( $12 \times 12$ ) was 1.35 mm, the edge of one line was 1.5 mm. In order to prevent the incidence photon of the edge of crystals back into the scintillator element [11], we designed a vertically edge with 2 mm length. The cross-sectional view of the 1.3-mm pitch detector  $18 \times 18$  scintillator array coupled to the  $14 \times 14$  element tapered light-guide is shown in Fig. 1c.

These R8900-C12 PSPMTs have many advantages, including high spatial resolution and output signals with location information. The 12 channels cross anodes (6 in the  $X$  direction and 6 in the  $Y$  direction) make them suitable for imaging applications. The PET detector comprised LYSO crystals and PSPMT coupled by silica gel and a readout circuit module to detect the gamma photons. The six channels of analog signals along the  $X$  and the  $Y$  directions were encoded into four analog signals  $A$ ,  $B$ ,  $C$ , and  $D$  by resistance-weighted circuits. The readout circuits of current PET detector module remains the same with the readout circuits of MicroPET F-220, which uses the Hamamatsu R5900-C12 PSPMTs, as shown in Fig. 1d.

In the experiment, we used a  $\pm 5 \text{ V}$  low-voltage source for the preamplifier board and a  $-750 \text{ V}$  high-voltage for the PSPMT. Each PET module processes four channel signals for crystal identification:  $A$ ,  $B$ ,  $C$ , and  $D$ . The position and energy of the incident gamma photons can be calculated by the equations as follow.

$$X = \frac{A}{(A + B)}, \quad (1)$$

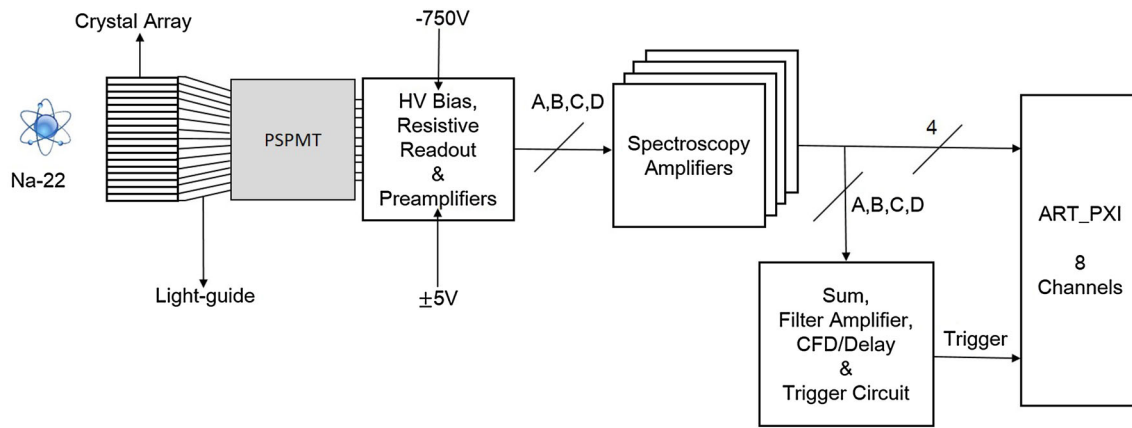


Fig. 2 Block diagram of the data acquisition system used to characterize detector response

$$Y = \frac{C}{(C + D)}, \tag{2}$$

and

$$E = A + B + C + D. \tag{3}$$

**Data acquisition system**

The PXI data acquisition (DAQ) system that we chose has several advantages, including a large data throughput rate, a variety of triggers, and multiple signal synchronous acquisition ability. Figure 2 shows a block diagram of the data acquisition system used to characterize detector response. In the experiment, the four channel signal outputs were delivered into a CAEN N568E low-noise spectroscopy amplifier and divided into two groups. One group of signals was digitized by an ART PXI8501 synchronous acquisition card. The other group of fast signals went through a nuclear instrumentation module (NIM) crate to generate a trigger logic signal. The electronics chain included linear fan-in/fan-out (Phillips Electronics 744), constant fraction discrimination (ORTEC 935), and gate delay generation (Phillips Electronics 794).

The four channel-triggered signals were sampled by using the PXI and displayed online by using the NI LabVIEW software program. Several signal processing functions were used, including baseline restoration, signal resampling and filtering, and peak value detection. The sampling rate of the analog-to-digital converter was 1 MHz for each channel. We selected the rising edge trigger mode, and 30 samples were recorded for one signal waveform. The first four samples were used to average the baseline offset. Each channel has a different baseline offset, which could lead to the wrong signal peak value and cause an incorrect position calculation for the gamma rays. We resampled the recorded signal waveforms with a spline interpolation algorithm fitting at

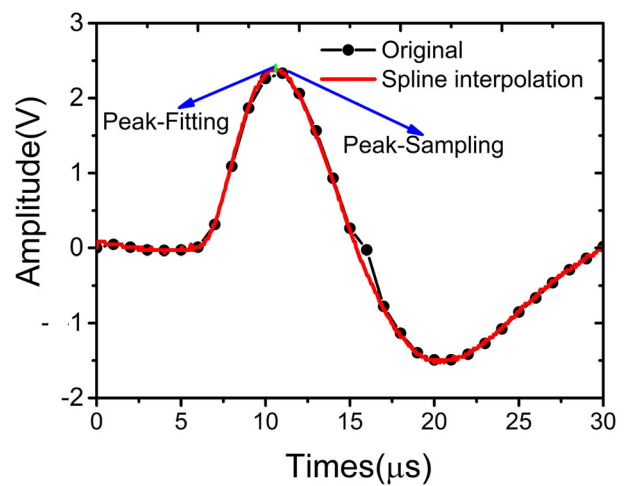


Fig. 3 Spline interpolation algorithm fitting of the PET detector module signal waveform

each moment to obtain the peak value, as shown in Fig. 3. Finally, a two-dimensional (2-D) position map of the LYSO crystal was displayed online according to the X and Y values calculated from the four signals of the PSPMT detector module.

**Results and discussion**

**Two-dimensional flood image**

When an event triggered, the digitized A, B, C, and D peak values are recorded in PXI ADQ system. The (X,Y) position of the event is then calculated by using the position equations. The (X,Y) value is used as an address to retrieve the region number of the pixels. The coordinates of each scintillation event are then transformed into a 256 × 256 matrix to obtain a 2-D position map, called the flood image. Figure 4 shows

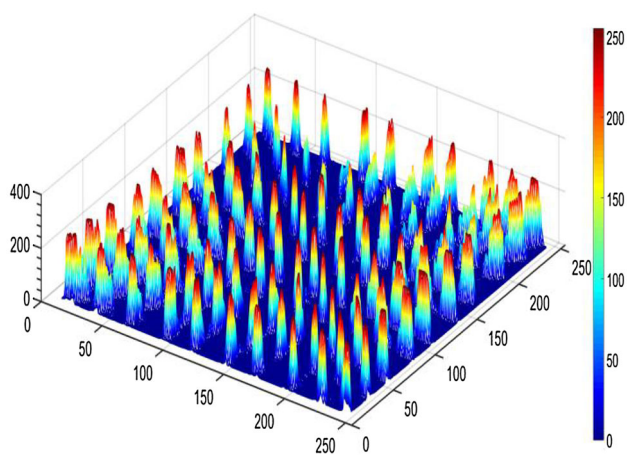


**Fig. 4** Crystal identification of the PET detector module by using 2.0-mm-pitch crystals

a crystal identification map of the PET detector module by using 2.0-mm-pitch LYSO crystals.

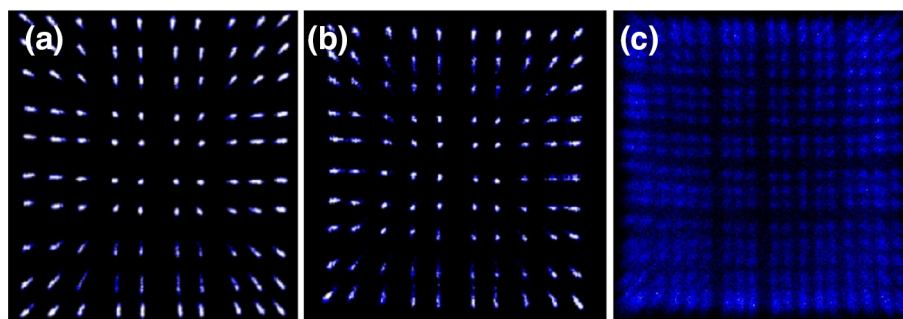
The flood image of the PET detector reflects the response of the LYSO scintillation crystal array to the gamma photons. When evaluating the performance of PET detectors, the first requirement is that the flood images of the crystals should be independently identified. The PET detector's flood images for the three different pitches are shown in Fig. 5.

Figure 5a, b indicate that the PET detector's flood images for the 2.0 and 1.6 mm pitches clearly reflect the  $10 \times 10$

independent crystal array and the good crystal division. For the PET detector with the 1.3 mm pitch, as shown in Fig. 5c, the flood image could show  $18 \times 18$  independent crystals, but was in poor quality. In order to improve the flood image quality of the 1.3-mm pitch detector, we would take into considerations from the following aspects. We will correct the non-uniform of crystal element response, use the high-speed uTCA DAQ system to record signal waveforms. The sampling frequency of the upcoming uTCA DAQ system is in two orders of magnitude compared with PXI. And the light-guide will be optimized in many ways, such as the materials, length, segmentation area and pixel size of the exit face. We will also measure the direct coupling of 1.3-mm pitch LYSO detector with PSPMT.

### Horizontal profile of the crystals

Crystal identification is one of the most important parameters for evaluate the performance of a PET detector in nuclear medicine imaging [12–14]. By acquiring flood images from the PET detector with all three pitches, we can create a horizontal profile of the crystals. In the experiment, we projected the data from a row in the crystal array onto the X-axis to collect statistics and performed a Gaussian fitting, as shown in Fig. 6.



**Fig. 5** PET detector's flood image for crystals with pitches of **a** 2.0 mm, **b** 1.6 mm, and **c** 1.3 mm

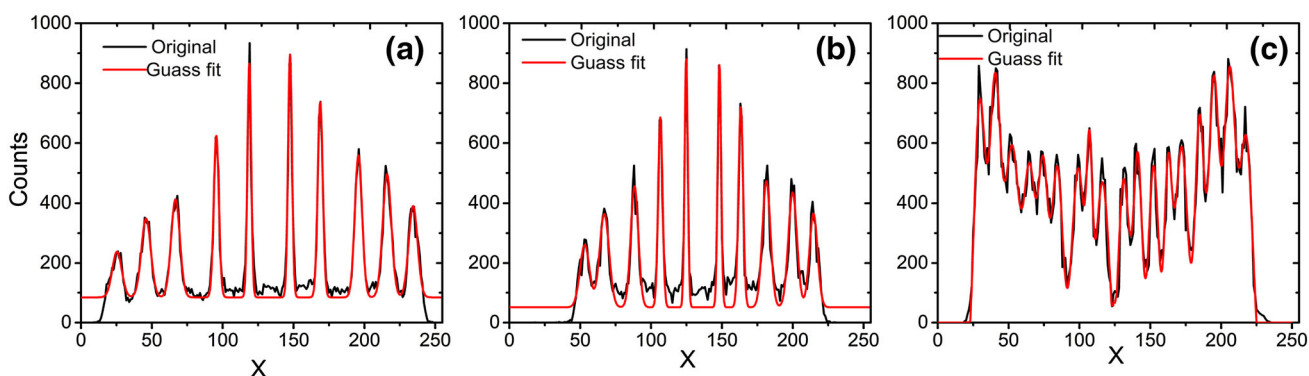


**Fig. 6** PET detector's profile for crystals with pitches of **a** 2.0 mm, **b** 1.6 mm, and **c** 1.3 mm

**Table 1** FWHM for all three pitches

Pitch (mm)	Average (mm)	Worst (mm)	Best (mm)
2.0	$0.46 \pm 0.03$	0.61	0.24
1.6	$0.32 \pm 0.03$	0.50	0.17
1.3	$0.21 \pm 0.02$	0.41	0.11

**Table 2** Energy resolution of the crystals for all three pitches

Pitch (mm)	Average (%)	Worst (%)	Best (%)
2.0	$16.8 \pm 1.76$	19.9	9.8
1.6	$20.1 \pm 2.24$	28.6	12.3
1.3	$31.5 \pm 3.76$	40.8	16.5

From Fig. 6, we can see that the identification of the crystals was good for all three pitches. We calculated the average full width at half maximum (FWHM) of each crystal’s profile, and FWHM of the crystals were  $0.46 \pm 0.03$ ,  $0.32 \pm 0.03$ , and  $0.21 \pm 0.02$  mm for the 2.0, 1.6, 1.3 mm pitches, respectively. The best FWHM values were 0.24, 0.17, and 0.11 mm, while the worst were 0.61, 0.50, and 0.41 mm, as listed in Table 1.

**Energy resolution**

To verify the PET detector response performance to the gamma photon energy, the energy spectrum of a 0.37 MBq Na-22 point source was measured for all three types of pitches. In this experiment, we recorded the energy spectrum and performed a Gaussian fitting of the crystal center and the crystal edge for the three different pitches. The ratio

of the FWHM and the peak position reflects the energy resolution of the detector [15]. As shown in Fig. 7, for the energy spectrum at the center of the crystals with 2.0 and 1.6 mm pitches, both the 511 keV peak and the 1.275 MeV peak could be clearly identified (Fig. 7a, b). For the energy spectrum at the edge of the crystals with 2.0 and 1.6 mm pitches, Fig. 7d, e shows only the 511 keV peak, and the 1.275 MeV peak was not very clear. The smallest crystal pitch was 1.3 mm; as shown in Fig. 7c, f, only the 511 keV peak could be clearly seen for the center and edge of the crystals.

We calculated the energy resolution of all three types of PET modules for 511 keV peaks. The average energy resolutions were  $16.8 \pm 1.76$ ,  $20.1 \pm 2.24$ , and  $31.5 \pm 3.76\%$  for the 2.0-, 1.6-, and 1.3-mm-pitch LYSO crystals, respectively. The best energy resolutions that the three pitches could achieve were 9.8, 12.3, and 16.5% and the worst energy resolutions were 19.9, 28.6 and 40.8%, as listed in Table 2.

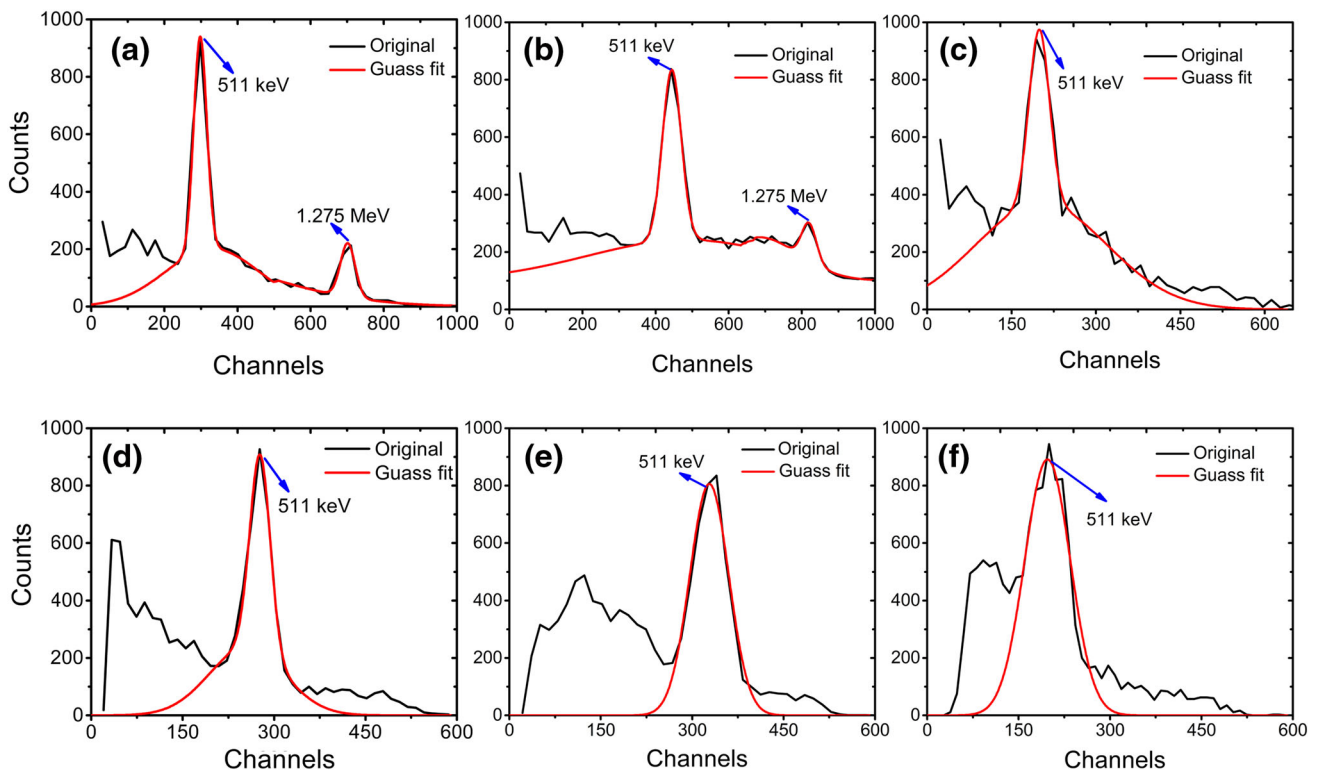


**Fig. 7** Energy spectrum at the crystal center for crystals with pitches of **a** 2.0 mm, **b** 1.6 mm, and **c** 1.3 mm. Edge energy spectrum for crystals with pitches of **d** 2.0 mm, **e** 1.6 mm, and **f** 1.3 mm

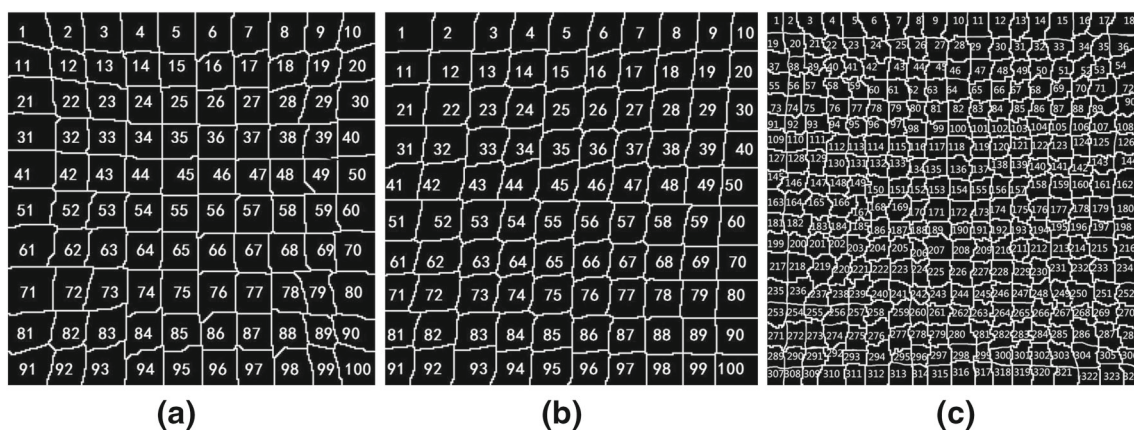


**Fig. 8** Crystal look-up tables for crystals with pitches of **a** 2.0 mm, **b** 1.6 mm, and **c** 1.3 mm

### Crystal look-up table

The crystal look-up table has a direct impact on imaging quality [16–18]. Currently, there are many kinds of crystal segmentation methods, such as watershed algorithms, Fourier-transform-based segmentation and segmentation algorithms based on data clustering. These methods entail direct processing of the position spectra obtained from the 2-D coordinate position of incident gamma events. To follow up the imaging of small-animal subjects, we used the crystal array look-up table and assigned a number for each pitch of the PET detector with the watershed algorithm, as shown in Fig. 8.

The characterizations of three LYSO PET detector modules with 2.0, 1.6 and 1.3mm pitches demonstrate that the tested LYSO crystal array detectors could be used in the small-animal PET imaging applications. In particular, for the 1.3-mm pitch LYSO detector, one could potentially achieve sub-millimeter small-animal PET image. Although we have optimized the light-guide design for the 1.3 mm pitch LYSO detector, and the  $18 \times 18$  crystal elements were independently identified, the detector quality still need be improved to produce high quality PET images using this detector.

### Conclusion

A prototype PET imaging experiment platform was developed and tested at laboratory; it comprised PET modules with LYSO crystals, light-guide and PSPMTs, NIM electronics, and a PXI DAQ system. We have measured the performance of three PET detectors (with 2.0, 1.6, and 1.3 mm LYSO crystals) using this setup with 1 MHz sampling frequency. Experimental results show that the flood image of 2.0 and 1.6 mm crystals with  $10 \times 10$  arrays could be distinguished independently, which were directly coupled to Hamamatsu R8900-C12 PSPMT. For the 1.3-mm-pitch crystal with an  $18 \times 18$  array, we used a tapered light-guide to obtain the

flood image. Results show that the light-guide design can clearly reflect the  $18 \times 18$  independent crystal array. However, further optimization of the 1.3-mm pitch detector was still needed for high-resolution system design. The FWHM values of the crystal horizontal profile can reach  $0.46 \pm 0.03$ ,  $0.32 \pm 0.03$ , and  $0.21 \pm 0.02$  mm for the 2.0-, 1.6-, and 1.3-mm-pitch LYSO crystals, respectively, while the average energy resolution can reach  $16.8 \pm 1.76$ ,  $20.1 \pm 2.24$ , and  $31.5 \pm 3.76\%$ . We got the crystal look-up table with the watershed algorithm. The PET detector modules of the 2.0, 1.6 and 1.3 mm LYSO crystal arrays could be potentially used in the small-animal PET imaging applications, and are promising to achieve sub-millimeter PET images.

**Acknowledgements** This work was supported by National Natural Science Foundation of China (11305083), and in part by the Fundamental Research Funds for the Central Universities under Grant lzujbky-2016-27. The authors would like to thank Dr. XU ZhiGuo of Institute of Modern Physics (IMP), Chinese Academy of Science for his valuable discussions.

### References

1. S.R. Cherry, In vivo molecular and genomic imaging: new challenges for imaging physics. *Phys. Med. Biol.* **49**, R13–R48 (2004)
2. M.E. Phelps, Positron emission tomography provides molecular imaging of biological processes. *Proc. Natl. Acad. Sci.* **97**, 9226–33 (2000)
3. J. Seidel, J.J. Vaquero, S. Siegel, W.R. Gandler, M.V. Green, Depth identification accuracy of a three layer phoswich PET detector module. *IEEE Trans. Nucl. Sci.* **46**(3), 485–490 (1999)
4. A. Saoudi, C.M. Pepin, F. Dion, M. Bentourkia, R. Lecomte, M. Andreaco et al., Investigation of depth-of-interaction by pulse shape discrimination in multicrystal detectors read out by avalanche photodiodes. *IEEE Trans. Nucl. Sci.* **46**(3), 462–467 (1999)
5. J.B. Mosset, O. Devroede, M. Krieguer, M. Rey, J.M. Vieira, J.H. Jung et al., Development of an optimized LSO/LuYAP phoswich detector head for the Lausanne ClearPET demonstrator. *IEEE Trans. Nucl. Sci.* **53**(1), 25–29 (2006)
6. R. Pain, R. Pellegrini, P. Bennati et al., A novel parallel hole collimator for high resolution SPET imaging with a compact LaBr3

- gamma camera, in 2008 IEEE NSS/MIC Conference Record, pp. 3824–3828
7. K. Xiaowen, W. Shi, L. Yaqiang, X. Sun, R. Zhou, T. Ma, Z. Wu, Y. Jin, A simple smart time-to-digital convertor based on vernier method for a high resolution LYSO MicroPET, in Presented at Nuclear Science Symposium Conference Record, 2007. NSS '07. IEEE (2007)
  8. C.Y. Liu, A.L. Goertzen, Improved event positioning in a gamma ray detector using an iterative position-weighted centre-of-gravity algorithm. *Phys. Med. Biol.* **58**, N189–N200 (2013)
  9. Q. Xie et al., Implementation of LYSO/PSPMT block detector with all digital DAQ system. *IEEE Trans. Nucl. Sci.* **60**, 1487–1494 (2013)
  10. L. Wang, J. Zhu, X. Liang et al., Performance evaluation of the Trans-PET® BioCalibur® LH system: a large FOV small-animal PET system. *Phys. Med. Biol.* **60**, 137–150 (2015)
  11. R.A. Mintzer, S.B. Siegel, Design and performance of a new pixelated LSO/PSPMT gamma-ray detector for high resolution PET imaging, in 2007 IEEE . Nucl. Sci Conference Record, pp. 3418–3422
  12. S. Surti, J.S. Karp, L.M. Popescu, M.E. Daube-Witherspoon, M. Werner, Investigation of time-of-flight benefit for fully 3-D PET. *IEEE Trans. Nucl. Sci.* **25**(5), 529–538 (2006)
  13. Z. Gu, D.L. Prout, R.W. Silverman et al., A DOI detector with crystal scatter identification capability for high sensitivity and high spatial resolution PET imaging. *IEEE Trans. Nucl. Sci.* **62**(3), 740–747 (2015)
  14. S. Krishnamoorthy, M.E. Werner, B. LeGeyt et al, Initial imaging results from a high spatial-resolution time-of-flight PET detector designed for dedicated breast imaging, in 2013 IEEE NSS/MIC Conference Record, pp. 1–6
  15. J.W. Son, M.S. Lee, J.S. Lee, A depth-of-interaction PET detector using a stair-shaped reflector arrangement and a single-ended scintillation light readout. *Phys. Med. Biol.* **62**, 465–483 (2017)
  16. Q. Wei, X. Li, T. Ma et al., A neighborhood standard deviation based algorithm for generating PET crystal position maps, in 2014 IEEE NSS/MIC Conference Record, pp. 1–4
  17. L. Vincent, L. Vincent, P. Soille, Watersheds in digital spaces: an efficient algorithm based on immersion simulations. *Trans. Pattern Anal. Mach. Intell.* **13**, 583–598 (1991)
  18. A.J. Chaudhari, A.A. Joshi, S.L. Bowen et al., Crystal identification in positron emission tomography using nonrigid registration to a Fourier-based template. *Phys. Med. Biol.* **53**, 5011–5027 (2008)